CELL BIOLOGY

Cellular stiffness sensing through talin 1 in tissue mechanical homeostasis

Manasa Chanduri[1]†, Abhishek Kumar[1]†, Dar Weiss[2], Nir Emuna[2], Igor Barsukov[3], Miusi Shi[1]‡, Keiichiro Tanaka[1], Xinzhe Wang[4], Amit Datye[4], Jean Kanyo[5], Florine Collin[5], TuKiet Lam[5,6], Udo D. Schwarz[4,7], Suxia Bai[8], Timothy Nottoli[8], Benjamin T Goult[3,9], Jay D. Humphrey[2], Martin A. Schwartz[1,2,10]*

Tissue mechanical properties are determined mainly by the extracellular matrix (ECM) and actively maintained by resident cells. Despite its broad importance to biology and medicine, tissue mechanical homeostasis remains poorly understood. To explore cell-mediated control of tissue stiffness, we developed mutations in the mechanosensitive protein talin 1 to alter cellular sensing of ECM. Mutation of a mechanosensitive site between talin 1 rod-domain helix bundles R1 and R2 increased cell spreading and tension exertion on compliant substrates. These mutations promote binding of the ARP2/3 complex subunit ARPC5L, which mediates the change in substrate stiffness sensing. Ascending aortas from mice bearing these mutations showed less fibrillar collagen, reduced axial stiffness, and lower rupture pressure. Together, these results demonstrate that cellular stiffness sensing contributes to ECM mechanics, directly supporting the mechanical homeostasis hypothesis and identifying a mechanosensitive interaction within talin that contributes to this mechanism.

INTRODUCTION

The extracellular matrix (ECM) is the primary determinant of mechanical properties and structural integrity of most tissues. Maintaining ECM is essential to normal tissue function such that adverse changes to ECM mechanics reflect and contribute to pathological remodeling in diverse diseases including cancer, pulmonary fibrosis, and kidney failure, among many others (*1*–*3*). This connection between ECM organization and mechanics is especially crucial in the cardiovascular system. Heart failure is closely associated with fibrosis of cardiac tissue while stiffening of central arteries is a substantial causative factor in cardiovascular, neurovascular, and renovascular disease (*4*). Abnormal ECM remodeling plays a central role in aneurysms, the abnormal dilatation of large arteries that predisposes to often-fatal dissection and rupture (*5*). Ascending thoracic aortic aneurysms (TAAs) in particular are principally caused by mutations in genes that code for ECM proteins such as fibrillin-1 (*6*, *7*), contractile proteins such as smooth muscle α-actin (*7*, *8*) and myosin (*9*), and upstream regulators of their expression and function such as TGFβ receptors (*10*) and myosin light chain (MLC) kinase (*11*).

The compositional and organizational features of ECM that dictate mechanical properties are relatively constant over many decades of adult human life despite the continual turnover of cells and most ECM components (*1*, *12*). This observation has given rise to the concept of tissue mechanical homeostasis (*4*), whereby cells sense mechanical loads and properties of the ECM and adjust rates of matrix synthesis, assembly, and degradation to maintain healthy tissue. Failure of these mechanisms is central to compromised function and disease progression. The best evidence for homeostasis probably comes from studies of arteries, where changes in blood pressure that change circumferential stress leads to changes in wall thickness that restore wall stress to nearly the original values (*13*). We recently reported a role for microRNAs (miRNAs) in vascular endothelial cells, such that stiff environments up-regulate a network of miRNAs that limit expression of contractile, adhesion, and ECM proteins that promote tissue stiffening (*14*). Nevertheless, despite its conceptual appeal, experimental evidence supporting the concept of tissue mechanical homeostasis and mechanistic insights are sparse.

ECM stiffness is sensed by cells via transmembrane integrins and associated cytoskeletal linkers, adapters, and signaling proteins, which can modulate intracellular biochemical pathways to elicit homeostatic responses (stiffness sensing) (*15*). The load-bearing integrin-cytoskeleton linker talin 1 (hereafter talin) is a mechanosensitive protein that contains domains that unfold and refold in response to tension (*16*–*22*). Changes in ECM or substrate stiffness determine the force applied to talin through modulation of contractile forces exerted by the cell (*18*), consistent with its role in stiffness sensing.

Talin contains a long, C-terminal rod domain consisting of sequential α helix bundles, termed R1 through R13, that exhibit spring-like behavior, unfolding under tension and refolding when tension diminishes (*16*, *17*). These domains function as bidirectional switches, wherein specific molecular interactions or signaling pathways are turned on or off by tension (*23*). Most prominently, vinculin binds to specific sites within many of the helix bundles (*24*), which reinforces the connection to actin under tension (*19*).

[1]Yale Cardiovascular Research Center, Cardiovascular Medicine, Department of Internal Medicine, Yale School of Medicine, Yale University, New Haven, CT 06511, USA. [2]Department of Biomedical Engineering, Yale University, New Haven, CT 06510, USA. [3]Department of Biochemistry, Cell and Systems Biology, Institute of Systems, Molecular and Integrative Biology, University of Liverpool, Crown Street, Liverpool L69 7ZB, UK. [4]Department of Mechanical Engineering and Materials Science, Yale University, New Haven, CT 06511, USA. [5]Keck MS & Proteomics Resource, Yale University School of Medicine, New Haven, CT 06510, USA. [6]Department of Molecular Biophysics and Biochemistry, Yale University, New Haven, CT 06510, USA. [7]Department of Chemical and Environmental Engineering, Yale University, New Haven, CT 06510, USA. [8]Department of Comparative Medicine, Yale University School of Medicine, New Haven, CT 06520, USA. [9]School of Biosciences, University of Kent, Canterbury, UK. [10]Department of Cell Biology, Yale School of Medicine, New Haven, CT 06511, USA.
*Corresponding author. Email: martin.schwartz@yale.edu
†These authors contributed equally to this work.
‡Present address: State Key Laboratory of Oral and Maxillofacial Reconstruction and Regeneration, Key Laboratory of Oral Biomedicine Ministry of Education, Hubei Key Laboratory of Stomatology, School and Hospital of Stomatology, Wuhan University, Wuhan, China.

Deletion of talin or segments of the rod domain alters cellular mechanoresponses (*25*–*27*). However, these large perturbations also alter integrin-mediated adhesion and signaling more generally and, thus, are poorly suited to studying mechanical homeostasis in vivo. Here, we sought to test the contribution of cellular stiffness sensing to tissue mechanical homeostasis by developing mutations in talin that quantitatively shift stiffness sensing parameters without otherwise perturbing function. We generated mutations that mildly destabilize individual helix bundles. These experiments led to identification of the R1R2 interface as a previously unknown mechanosensitive site that regulates cellular stiffness sensing through its interaction with ARPC5L, an alternative component of the ARP2/3 complex. Mice bearing these mutations show altered ECM and mechanical properties in the ascending aorta. Together, these results identify a distinct talin-dependent mechanotransduction mechanism and demonstrate that cellular stiffness sensing is critical for tissue mechanical homeostasis.

RESULTS

Talin rod mutations

To investigate talin's role in cellular mechanosensing and tissue homeostasis, we introduced mutations into individual rod-domain helix bundles to decrease their stability though retaining their conformation at 37°C. Talin helix bundles are held together mainly by hydrophobic interactions within the core; thus, key hydrophobic amino acids were converted to more hydrophilic residues in the R1R2 (L638D, L716T, A718D, and V722R), R3 (I805T), and R10 (L1923A) domains to generate three destabilized talin rod-domain mutants (Fig. 1A). These domains were chosen because they contain well documented vinculin binding sites and are outside the actin and integrin binding and autoregulatory regions and, thus, should not otherwise perturb function. We performed circular dichroism to determine the thermodynamics of unfolding of the mutants in comparison to the wild-type (WT) domains. The indicated mutations led to moderate leftward shifts of the melting curves (Fig. 1, B and C, and fig. S1A), with minimal perturbation at 37°C. These mutations should thus lower the force required for unfolding.

Focal adhesion morphology and fibronectin deposition

These mutations were introduced into full-length talin containing the tension-sensor module to allow measurement of force across the molecule (*18*). Constructs were expressed in *Tln1*$^{-/-}$ mouse embryonic fibroblasts (MEFs) at close to endogenous levels (fig. S1B). All mutants localized to focal adhesions as expected (Fig. 2A). Cells expressing the R1R2 mutant had larger adhesions (Fig. 2, A and B) compared to WT talin, whereas R3 and R10 mutants were similar to WT. The R1R2 mutant also showed increased recruitment to focal adhesions (Fig. 2C). Assessment of protein turnover within focal adhesions by fluorescence recovery after photobleaching (FRAP) showed no differences between the R1R2 mutant and WT (Fig. 2D and fig. S2A). Moreover, phosphorylation of focal adhesion kinase (FAK) and MLC were also unaffected, suggesting no change in focal adhesion signaling under these conditions (fig. S2, B to E).

Most of the cells expressing the R1R2 mutant showed large, elongated central adhesions (Fig. 2A) suggestive of fibrillar adhesions (*28*). We therefore stained for the fibrillar adhesion marker tensin1. R1R2 mutant cells showed increased tensin1 within the central adhesions (Fig. 2E and fig. S3A). No changes in tensin1 staining were observed with other mutants. Because fibrillar adhesions are sites of fibronectin deposition and matrix assembly (*28*), cells were stained for fibronectin. Cells expressing the R1R2 mutant showed increased fibronectin fibrils (Fig. 2F and fig. S3B) and increased fibronectin deposition by Western blotting (fig. S3, C and D). The results indicate that under conditions of cell culture, R1R2 stability regulates adhesion size, formation of fibrillar adhesions, and fibronectin fibrillogenesis.

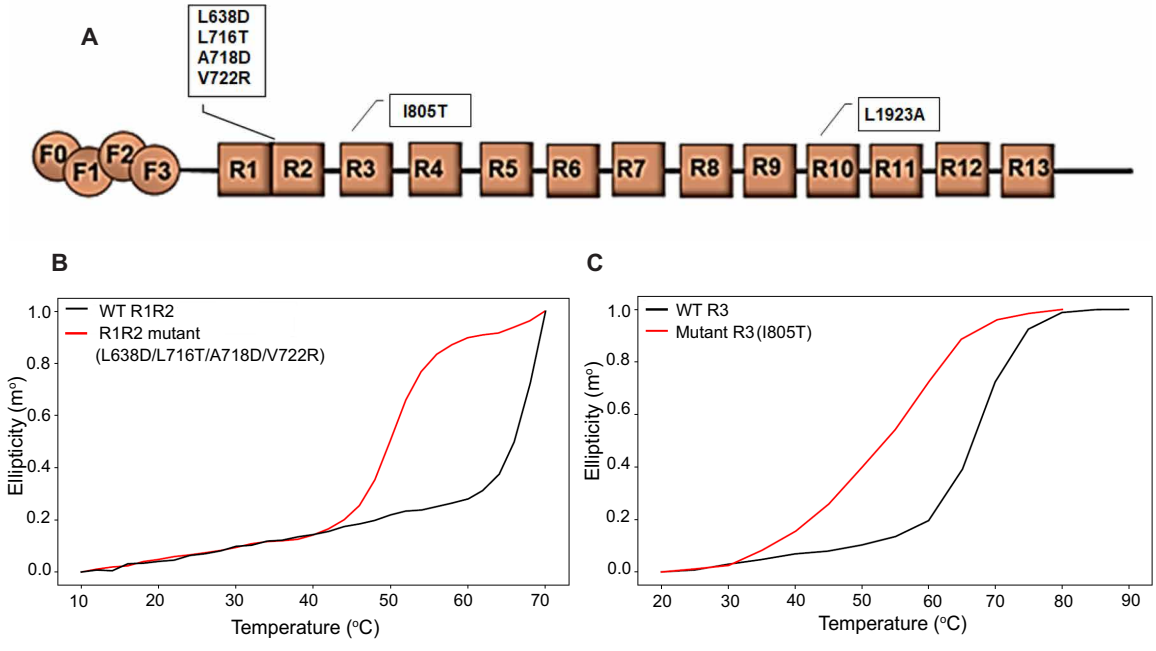

Fig. 1. Mutations in rod domains alter their stability. (**A**) Domain organization of talin showing destabilizing mutations introduced into the R1R2, R3, and R10 domains. (**B** and **C**) CD spectra showing molar ellipticity at a wavelength of 220 nm versus temperature in R1R2 (B) and R3 (C) mutant fragments compared to WT fragments.

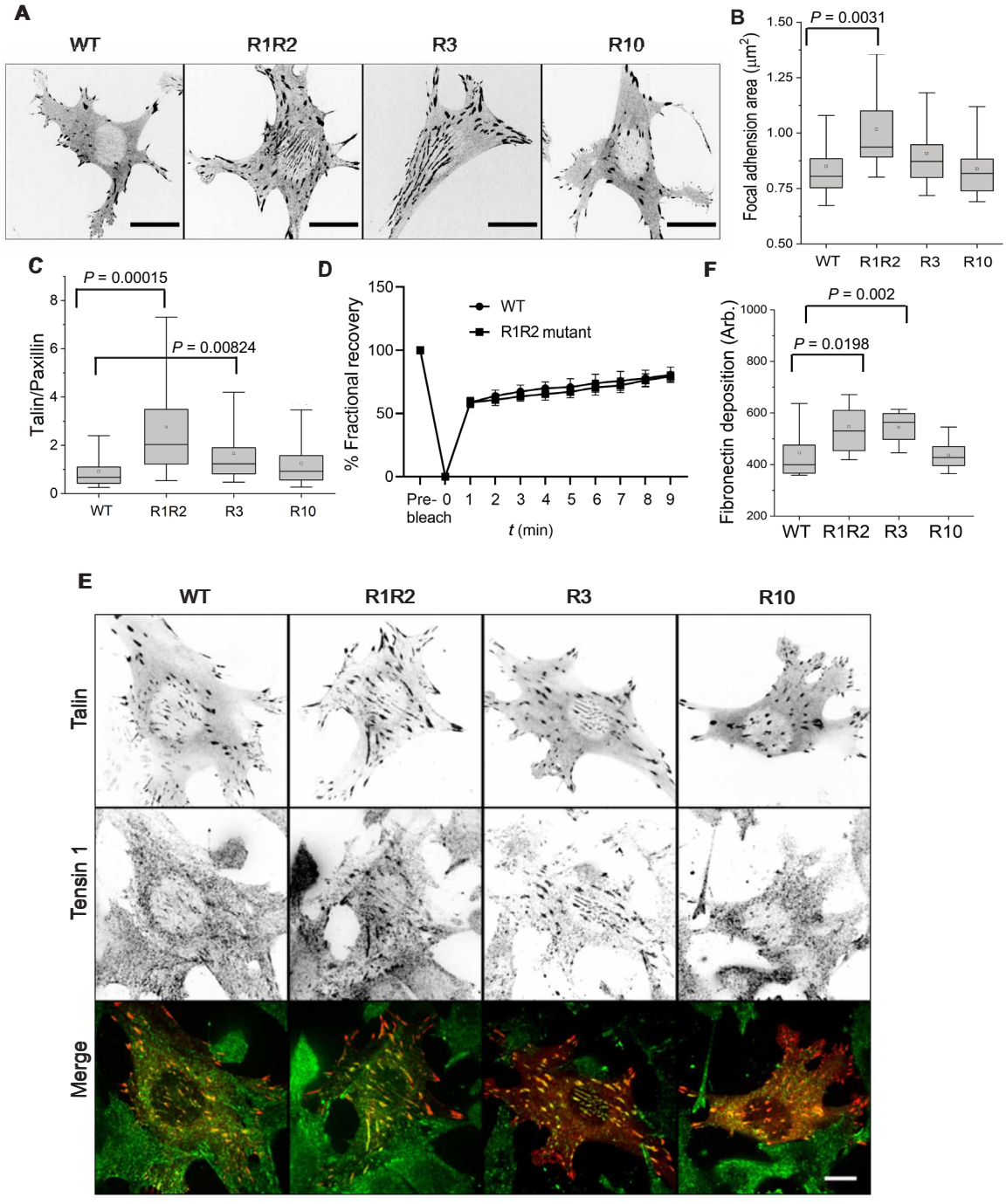

Fig. 2. Effects of rod-domain mutations on focal adhesions. (**A**) Representative intensity-inverted images showing focal adhesions in *Tln1*$^{-/-}$ MEFs expressing WT and rod-domain mutants plated for 3 hours on a fibronectin-coated glass bottom dish. Scale bars, 20 μm. (**B**) Quantification of focal adhesion area in (A). $N = 25$ cells for each sample. Boxes represent 25th to 75th percentile, whiskers represent 10th to 90th percentile, lines denote the median, and dots represent the mean. Statistics were analyzed by one-way ANOVA with Kruskal-Wallis post hoc test. (**C**) Quantified ratio of talin to paxillin within focal adhesions. $N = 25$ cells in each box plot. Boxes represent 25th to 75th percentile, whiskers represent 10th to 90th percentile, lines denote the median, and dots represent the mean. Statistics were analyzed by one-way ANOVA with Kruskal-Wallis post hoc test. (**D**) FRAP time course for WT and R1R2 mutant talin within individual focal adhesions. Data are means of % signal relative to starting values ± SEM. $N = 10$ cells per sample. (**E**) Representative immunofluorescence images of tensin-1 (green) in *Tln1*$^{-/-}$ MEFs expressing WT and rod-domain mutants (red) plated on glass for 48 hours. (**F**) Quantification of mean fibronectin intensity per cell in *Tln1*$^{-/-}$ MEFs expressing WT or mutant talin forms. $N = 15$ fields of view from three experiments. Boxes represent 25th to 75th percentile, whiskers represent 10th to 90th percentile, lines denote the median, and dots represent the mean. Statistics were analyzed by one-way ANOVA with Kruskal-Wallis post hoc test.

R1R2 mutant force transmission and substrate stiffness sensing

Unfolding of R1R2 domains is expected to recruit more vinculin, strengthening the link to F-actin and increasing force transmission. We therefore assessed mechanical loading using our previously described fluorescence resonance energy transfer (FRET) sensor (*18*), for which lower FRET indicates higher tension. When plated on glass coverslips, the talin R1R2 mutant showed decreased FRET (Fig. 3A), indicating increased tension, while the other mutants were comparable to WT.

Cell sensing of substrate stiffness has been linked to talin (*18*, *25*) and domain opening could be expected to alter this behavior. Cells expressing WT versus mutant talin constructs were therefore plated on fibronectin-coated polyacrylamide hydrogels with varying stiffness and cell morphology was assessed. Cells containing the R3 and R10 mutant showed the expected increase in cell area with increasing substrate stiffness comparable to WT talin (Fig. 3B). By contrast, the R1R2 mutant induced a distinct leftward shift in the curve, such that these cells were fully spread on compliant/soft 3-kPa substrates, whereas control cells required 30 kPa (stiff substrate) to reach a similar spread area (Fig. 3B and fig. S4A). The R1R2 mutant–expressing cells also were less circular on 3 kPa as compared to WT talin cells (fig. S4B). To determine whether this shift led to changes in signaling, we examined Yes-associated protein (YAP)/transcriptional coactivator with PDZ binding motif (TAZ), transcription factors that undergo stiffness-dependent nuclear translocation and control subsequent cellular responses (*29*). Talin R1R2 mutant cells also increased YAP/TAZ nuclear-to-cytoplasmic ratio on the 3-kPa substrate (Fig. 3C and fig. S4C). We next examined traction stress in cells on 3- versus 30-kPa substrates. Cells increase traction forces as a function of spread area (*30*). However, expressing these tractions as stress (force/unit area) corrects for the contribution from higher spreading, allowing assessment of area-independent effects (Fig. 3D and fig. S4D). Traction stress in R1R2 mutant cells also showed a leftward shift, with higher stress on surfaces of intermediate stiffness. Together, these results provide strong evidence that the R1R2 mutant alters cell substrate stiffness sensing.

Vinculin-dependent and independent effects

Helix bundle unfolding promotes vinculin binding (*16*, *31*) and increases the tension on talin (*18*, *32*). To test the requirement for vinculin in these effects, WT and R1R2 mutant talin were expressed in talin and vinculin double-knockout cells (fig. S5A) and the above parameters were assessed in cells plated on glass coverslips. Loss of vinculin abolished the difference in tension on talin between the WT and R1R2 mutant in cells lacking endogenous talin 1 (Fig. 4A). However, there was only a partial rescue of focal adhesion size. When examined on

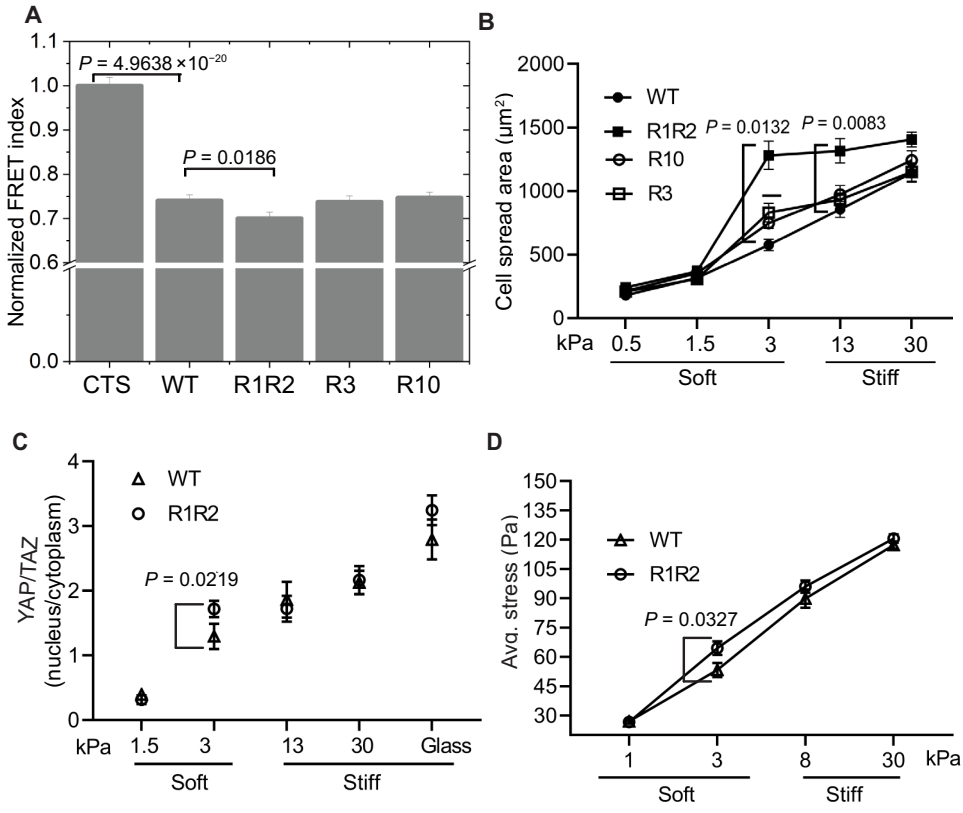

Fig. 3. Effect of talin mutation on tension and stiffness sensing. (**A**) FRET index of WT and mutant talin in focal adhesions normalized to a C-terminal Talin sensor (CTS) control. Values are means ± SEM of $N = 59$ to 77 cells from three independent experiments. Statistics were analyzed by one-way ANOVA Kruskal-Wallis post hoc test. (**B**) Quantification of spread area of cells expressing WT and talin mutants on polyacrylamide gels of varying stiffness. Values are means ± SEM of $N = 52$ to 78 cells. Statistics analyzed by two-way ANOVA with Tukey's post hoc test. (**C**) Quantification of YAP localization in cells expressing WT and R1R2 mutant talin on compliant substrates. Values are mean ± SEM of $N = 25$ cells per sample. Statistics analyzed by two-way ANOVA with Tukey's post hoc test. (**D**) Average stress (force per unit area) in WT- and R1R2 mutant–expressing cells on 3- and 30-kPa substrates. Values are mean ± SEM of $N = 25$ cells. Statistics analyzed by two-way ANOVA with Tukey's post hoc test.

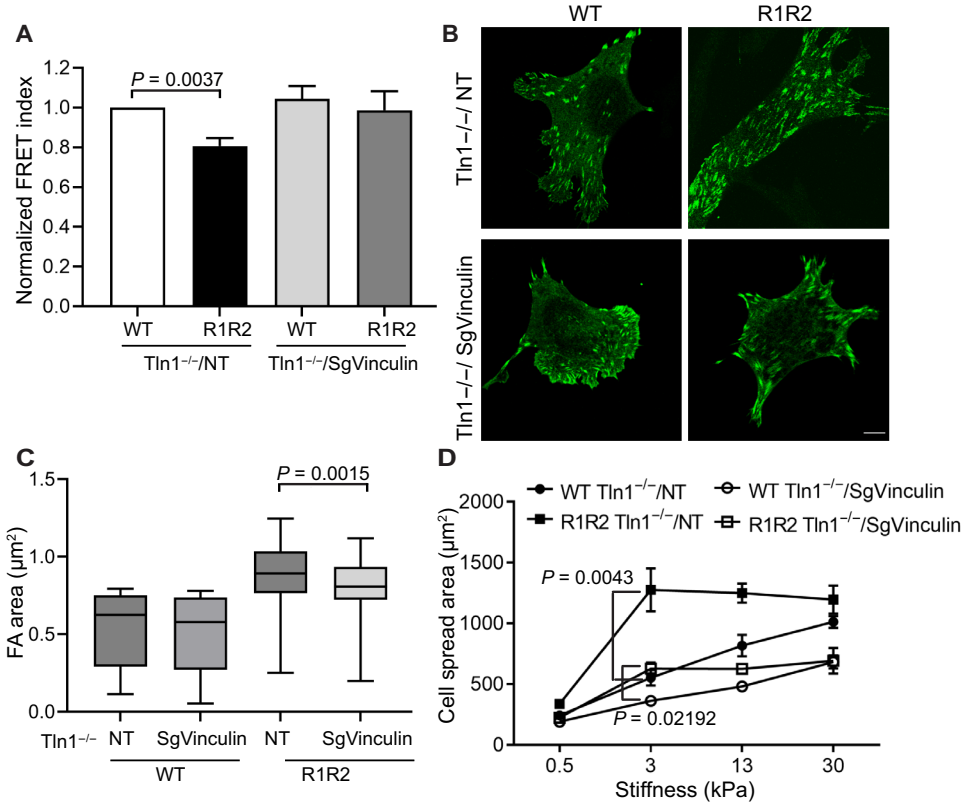

Fig. 4. Effect of vinculin depletion on R1R2 mutant phenotypes. (**A**) Normalized FRET index of WT and R1R2 mutant talin expressed in *Tln1*$^{-/-}$ MEFs with vinculin depletion by guide RNA against vinculin (*Tln1*$^{-/-}$/SgVinculin) or *Tln1*$^{-/-}$ MEFs with control nontargeting gRNA (NT). Values are means ± SEM, $N = 25$ cells. Statistics analyzed by one-way ANOVA with Kruskal-Wallis post hoc test. (**B**) Representative images of WT- and R1R2-expressing *Tln1*$^{-/-}$ and Tln1$^{-/-}$/SgVinculin MEFS. Scale bar, 5 μm. (**C**) Focal adhesion area in *Tln1*$^{-/-}$ and Tln1$^{-/-}$/SgVinculin MEFS. Boxes represent 25th to 75th percentile, whiskers represent 10th to 90th percentile, and lines denote the median. Statistics analyzed by one-way ANOVA with Kruskal-Wallis post hoc test. (**D**) Quantification of cell spread area in WT- or R1R2-expressing *Tln1*$^{-/-}$ and Tln1$^{-/-}$/SgVinculin MEFS. Values are means ± SEM of $N = 32$ to 54 cells. Statistics were analyzed by two-way ANOVA with Tukey's post hoc test.

polyacrylamide gels, vinculin depletion diminished maximal spread area but the shift in the stiffness sensing curve with the R1R2 mutant was preserved, with spreading still maximal on 3-kPa substrates (Fig. 4, B to D). These results reveal both vinculin-dependent (talin tension) and vinculin-independent (stiffness sensing) effects, with focal adhesion size showing components of both. These findings suggest the existence of tension-dependent effectors of R1R2 unfolding other than vinculin.

Critical role for the R1R2 interface

The R1 and R2 domains are uniquely organized, with R1 and R2 making a side-to-side contact in addition to the end-to-end contact that occurs in all domains (*31*). The above effects might thus be due to opening of either the R1R2 interface or the R2 helix bundle core. To address this question, we developed four additional R1R2 domain mutants: two mutants (L682T/V747T and L716T/L682T/V747T) that target the R2 internal core interactions (Fig. 5A and fig. S5B) and two (L638D/V722R and L638D/A718D/V722R) that target the R1R2 interface (fig. S5B). These mutations were introduced into full-length talin and expressed in *Tln1*$^{-/-}$ MEFs. When assayed for spreading on 3- versus 30-kPa substrates, only the R1R2 interface mutations increased spreading on the compliant substrate (Fig. 5B). The interface mutants also had larger adhesions (Fig. 5C). However, a change in tension on talin, indicated by FRET index, was not seen with either the core or interface mutations alone (Fig. 5D), indicating that this effect required both. As vinculin binding requires exposure of the helix bundle core, these results are consistent with findings from Fig. 4 that effects on cellular stiffness sensing and focal adhesion size occur through an effector other than vinculin.

Effectors of the R1R2 domain

To identify effectors that bind the R1R2 interface, we reasoned that proteins that bind the free R2 domain but not the R1R2 dimer would be potential effectors that interacted only after tension-dependent disruption of R1R2 binding. We therefore performed pull-downs from cell lysates expressing green fluorescent protein (GFP)–tagged R2 and GFP-tagged R1R2 domains, followed by mass spectrometric proteomics (table S1). More than 30 proteins preferentially bound the free R2 domain. These included multiple cytoskeletal proteins that are potential effectors of cellular mechanosensing (table S2). To narrow the search, we first assessed whether the effectors worked through F-actin or microtubules. Thus, stiffness-dependent cell spreading was assayed in the presence of the ARP2/3 inhibitor CK666, the formin inhibitor SMIFH2, and the microtubule inhibitor nocodazole. The R1R2 stiffness-sensing phenotype was reversed by CK666 (Fig. 6A). Nocodazole blocked stiffness sensing for both WT and mutant talin and, thus, was not informative, while the remaining drugs did not affect stiffness sensing. CK666 also partially reversed the large adhesion

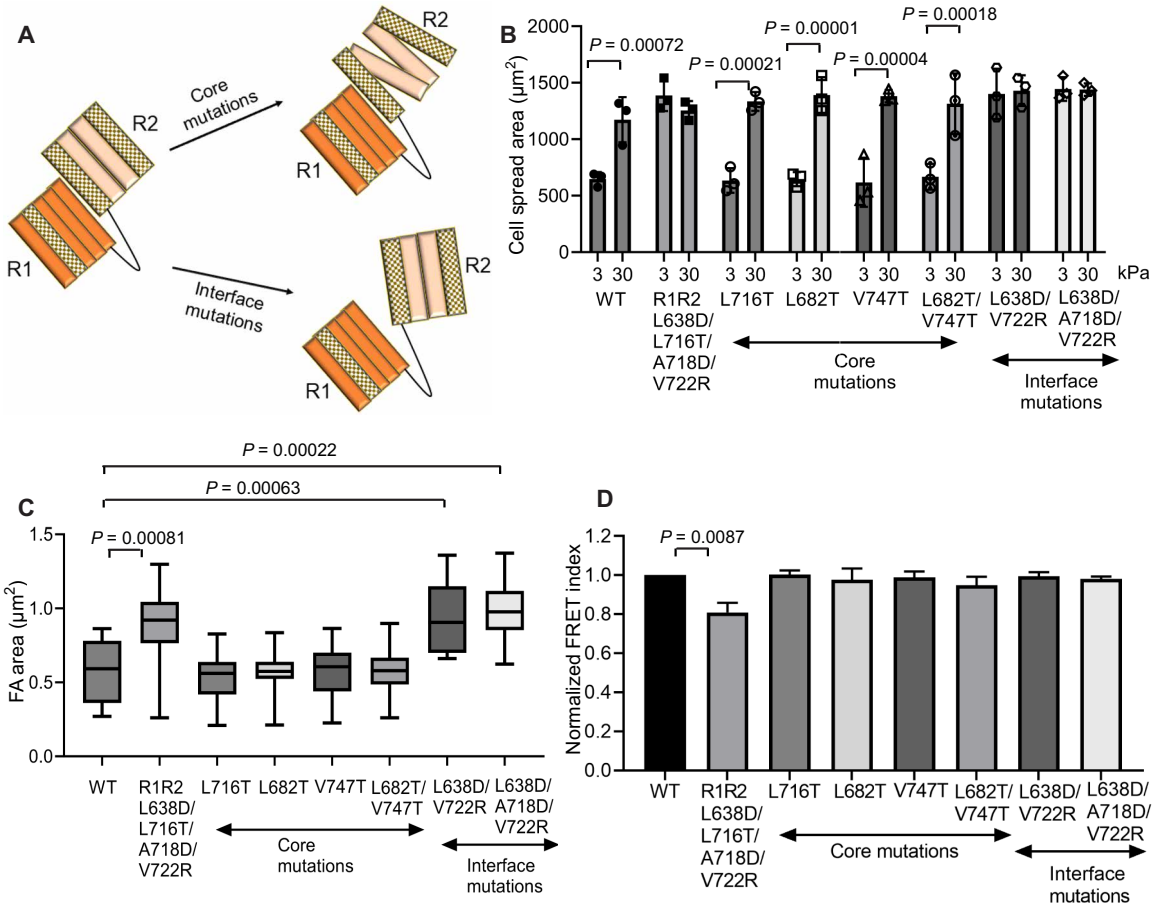

Fig. 5. Effects of R2 core versus R1R2 interface interactions. (**A**) Schematic of R2 core versus R1R2 interface mutations. (**B**) Cell spread area of WT and R1R2 core and interface talin mutants on 3- and 30-kPa substrates. Values are means ± SEM of $N = 3$ experiments. Statistics analyzed by one-way ANOVA with Kruskal-Wallis post hoc test. (**C**) Focal adhesion area of WT and R1R2 core and interface mutants in *Tln1*$^{-/-}$ MEFs. $N = 23$ to 28 cells. Statistics analyzed by one-way ANOVA with Kruskal-Wallis post hoc test. (**D**) Normalized FRET index of WT and R1R2 core and interface mutant talin in focal adhesions. Values are means ± SEM of $N = 25$ cells. Statistics were analyzed by one-way ANOVA with Kruskal-Wallis post hoc test.

size in cells expressing the R1R2 mutant talin but had no significant effect on cells expressing WT talin (Fig. 6, B and C).

These results led us to investigate ARPC5L, one of the proteins that specifically bound the R2 domain in the proteomic assay (table S2). ARPC5L is a component of the ARP2/3 complex that nucleates F-actin assembly. To confirm the interaction, GFP-tagged versions of WT and mutant R1R2, R1, and R2 domains were expressed in cells together with Flag-tagged ARPC5L or ARPC5 (a functional isoform of ARPC5L). Lysates were immunoprecipitated with GFP nanobody beads and analyzed by Western blotting. ARPC5L showed little association with WT R1R2 or WT R1 but significantly more with WT R2. ARPC5L showed higher association with the mutant R1R2 and with the mutant R2 domain. ARPC5 showed no binding to any of the talin constructs. These results support the notion that ARPC5L binding requires separation of the R1 and R2 domain and is specific to this isoform (Fig. 6D). To gain further insights, we used AlphaFold2 to computationally model these interactions. According to this computational model, the R2 domain binds well to ARPC5L, which is also seen with the ARP2/3 complex (fig. S6, A to D). Overlay of the R2-ARPC5L complex with R1R2 (Protein Data Bank accession no. 1sj8) showed that the predicted ARPC5L binding site on R2 is immediately adjacent to the R1R2 interface, but that there are clashes between the R1 domain and ARPC5L. With no complementarity between the overlapping sidechains, these results support the idea that R1 limits ARPC5L binding to R2 (fig. S6C). Modeling also showed that the R1R2-binding region on ARPC5L is absent from ARPC5, consistent with the observed binding specificity.

To functionally test this hypothesis, we depleted ARPC5L in cells expressing the R1R2 interface mutant (fig. S6E). ARPC5L knockdown reversed the altered stiffness sensing and adhesion size in the R1R2 mutant (Fig. 6, E to G). ARPC5L depletion in cells expressing WT talin also slightly but significantly decreased cell spreading on substrates of 6.8 to 13 kPa. Together, these results identify ARPC5L as a distinct effector of talin mechanosensitivity.

ECM mechanics of R1R2 interface mutant mice

To understand the effects of altered stiffness sensing at the organismal level, the interface mutations (L638D and V722R), corresponding to codons in exon 17 and 19, respectively, were introduced into C57BL/6 mice using homolog-directed CRISPR-Cas9 mutagenesis (Fig. 7A). As described in Materials and Methods, the mutations were introduced sequentially in mouse embryos using homology

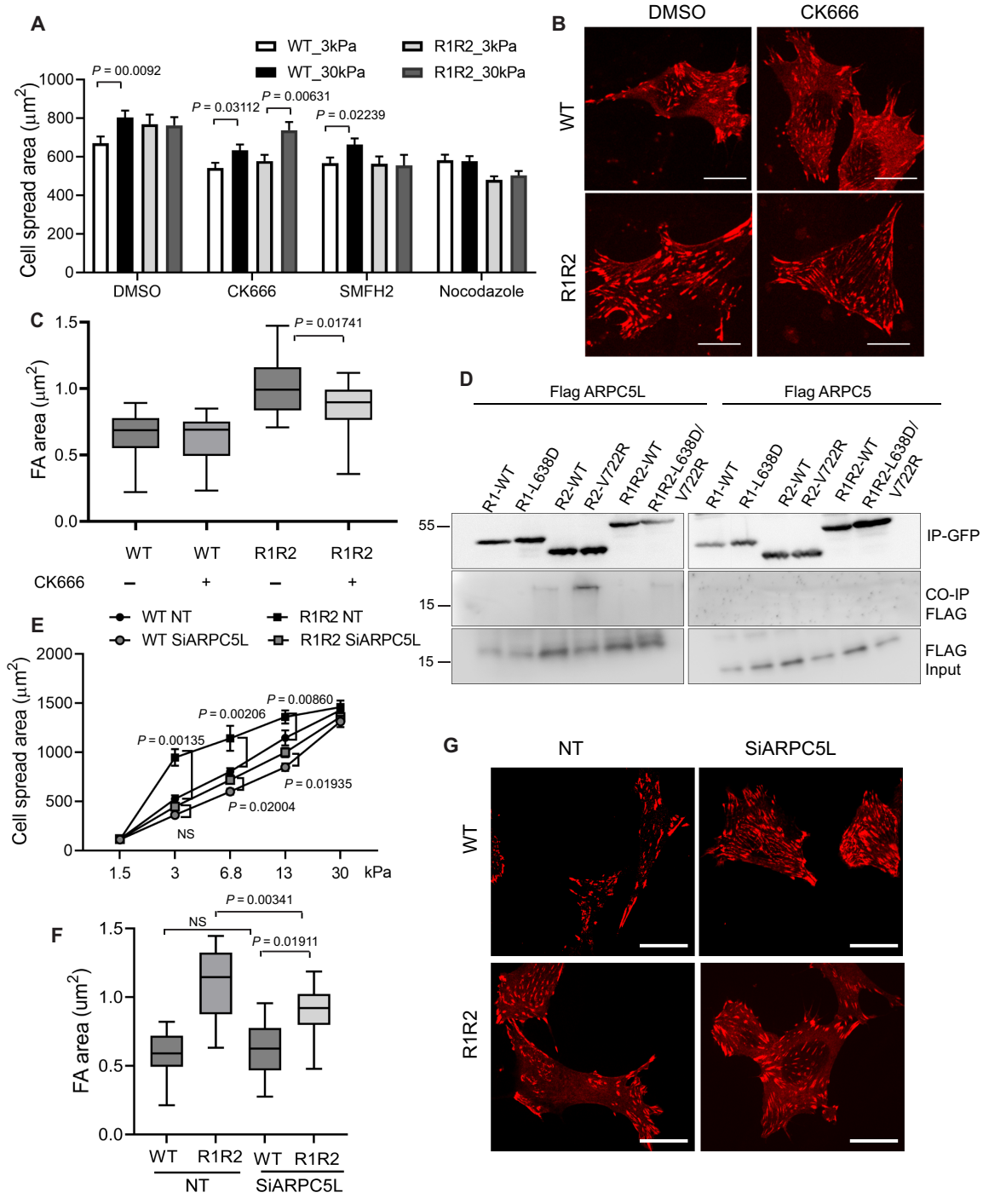

Fig. 6. ARPC5L mediates talin R1R2-dependent stiffness sensing. (**A**) Spread area in cells expressing WT talin versus destabilized mutant R1R2 talin on 3- and 30-kPa stiffness substrates in the presence of dimethyl sulfoxide (DMSO), ARP2/3 inhibitor (CK666), formin inhibitor (SMIFH2), and microtubule polymerization inhibitor (nocodazole). Values are means ± SEM of $N = 25$ to 50 cells. Statistics analyzed by one-way ANOVA with Kruskal-Wallis post hoc test. (**B**) Representative images showing focal adhesions with and without CK666 in cells expressing WT and R1R2 mutant. Scale bars, 10 μm. (**C**) Quantified focal adhesion area from (B). $N = 20$ to 25 cells. Statistics analyzed by one-way ANOVA with Kruskal-Wallis post hoc test. (**D**) Representative blots showing coimmunoprecipitation of Flag-tagged ARPC5L and Flag-tagged ARPC5 with the indicated GFP-tagged talin constructs. (**E**) Quantified cell spread area in WT- and R1R2-expressing cells with (SiARPC5L) and without ARPC5L depletion [nontargeting siRNA (NT)] on hydrogels of varying stiffness. Values are means ± SEM of $N = 25$ to 50 cells. Statistics analyzed by two-way ANOVA with Tukey's post hoc test. NS, not significant. (**F**) Quantification and (**G**) representative images of WT- and R1R2 mutant–expressing cells with and without ARPC5L depletion. Scale bars, 10 μm. $N = 37$ to 66 cells. Statistics analyzed by one-way ANOVA with Kruskal-Wallis post hoc test..

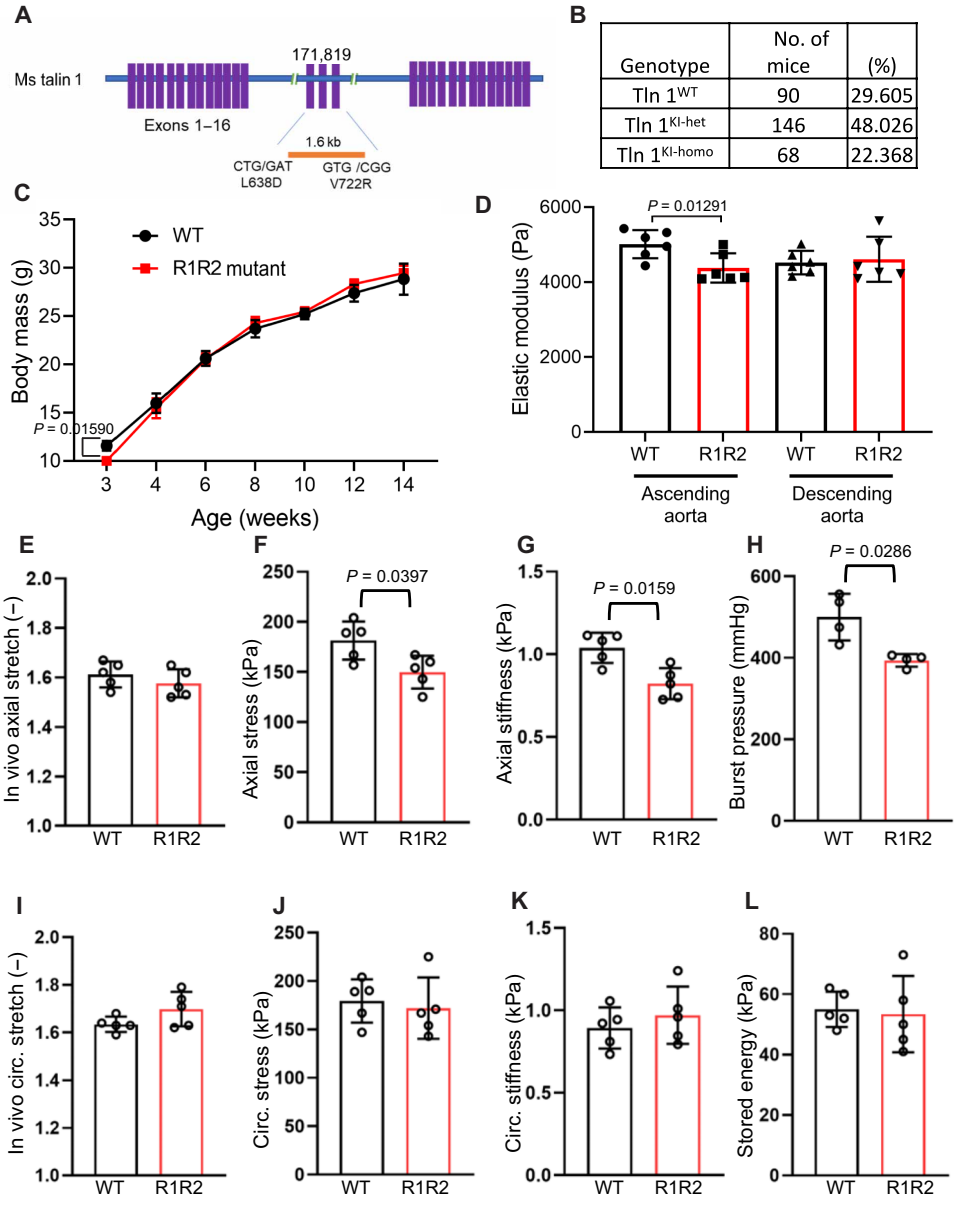

Genotype	No. of mice	(%)
Tln 1^{WT}	90	29.605
Tln 1$^{KI\text{-}het}$	146	48.026
Tln 1$^{KI\text{-}homo}$	68	22.368

Fig. 7. R1R2 mutant knock-in mice. (**A**) Schematic showing the insertion of L638D and V722R mutations in exon 17 and exon 19 using a 1.6-kb template. (**B**) Genotype of progeny from mating heterozygous *Tln1*$^{L638D\text{-}V722R/+}$ mice (*Tln1*$^{KI\text{-}het}$). χ^2 analysis revealed no significant difference. χ^2 equals 3.658 with 2 degrees of freedom. The two-tailed *P* value equals 0.1606 and is not statistically significant. (**C**) Body mass of WT and R1R2 mutant knock-in mice from 3 to 14 weeks of age. Values are means ± SEM. Statistics analyzed by unpaired *t* test. (**D**) Compressive radial stiffness of the ascending aorta of P24 WT and R1R2 mutant mice measured by atomic force microscopy applied from the adventitial surface. Values are means ± SEM of $N = 6$ mice. Statistics analyzed by unpaired *t* test. (**E** to **L**) Ex vivo biomechanical measurements of ascending aorta of P24 WT and R1R2 mutant mice $N = 4$ for (H) and $N = 5$ for (E) to (G) and (I) to (L).

templates, the embryos implanted into C57BL/6 female mice, and progeny containing knock-in mutations on both alleles were identified by polymerase chain reaction (PCR; fig. S7A). Homozygous knock-in mice bred from these founders (henceforth termed R1R2 mutant mice) were viable (Fig. 7B) and fertile (fig. S7B). Younger mice showed slightly lower body mass, but this difference disappeared by 4 weeks (Fig. 7C). As mutations in ECM and contractile proteins play a critical role in mechanical homeostasis of the ascending aorta (*4*), we carried out a mechanical analysis of this tissue. Atomic force microscopy (AFM) measurements on the ascending aorta from mice at postnatal day P24 revealed a lower compressive elastic modulus in the mutant tissue compared to WT littermates (Fig. 7D). Tensile wall stress and stiffness under biaxial loading at physiological levels (90 mmHg, specimen-specific in vivo extension) were lower in the axial, but not the circumferential direction in ascending aortas from R1R2 mutant mice and burst pressures were reduced (Fig. 7, E to L), though with no differences in elastic energy storage (~55 kPa), overall distensibility (3.9×10^{-3} mmHg^{-1}), or failure stress (1.5 to 1.8 MPa). Given strong biaxial coupling, there was a trend toward increased circumferential stretch in the R1R2 mutant aortas at typical

values for in vivo systolic and diastolic pressures that did not reach significance (Fig. 7I). To our surprise, comparable analysis of the descending thoracic aorta showed no differences (fig. S8). These results suggest that altering cellular stiffness sensing with the R1R2 mutation leads to reduced tissue stiffness in the ascending aorta.

ECM is the main determinant of the mechanical properties of the arterial wall (*4*, *33*). A change in stiffness thus points toward altered ECM. Histological analysis of fibrillar collagen by picrosirius red and Movat's pentachrome revealed reduced staining in the R1R2 mutant aorta in both the adventitial and medial layers (Fig. 8, A to C). Collagen III was also lower in the mutant tissues (fig. S9). Together, R1R2 mutation with altered stiffness sensing in cellulo results in reduced ECM deposition and decreased material stiffness in vivo in the mouse ascending aorta.

DISCUSSION

The goal of this study was to explore the connection between cellular stiffness sensing and tissue mechanical homeostasis, focusing on ECM as the main determinant of tissue stiffness. We approached this challenge by developing talin mutants in which the stability of specific rod-domain helix bundles was reduced, which should allow opening under lower tension. Of the domains considered, mutation of the R1R2 interface had the strongest effect, increasing cell spreading and traction forces on surfaces of two- to threefold lower stiffness. When introduced into mice, these mutations resulted in reduced stiffness and increased structural vulnerability of the ascending aorta that correlated with reduced fibrillar collagen. Thus, when cells (incorrectly) sense the ECM as too stiff, they decrease collagen content to reduce tissue stiffness. This outcome directly supports the concept that cellular stiffness sensing governs tissue mechanical homeostasis.

A second key finding is identification of the R1R2 interface as a force-dependent site. R2 that is released from the R1 interaction but still in its folded conformation can bind ARPC5L to promote cell spreading. Single-molecule experiments showed that an R1-R3 construct unfolded in three distinct steps with large-scale movements attributable to R3 at ~5 pN, R2 at ~13 pN, and R1 at ~22 pN, respectively (*34*). In addition, a smaller movement was observed at ~10 pN, before full opening of R1 or R2 [figure 3, A and E, in (*34*)].

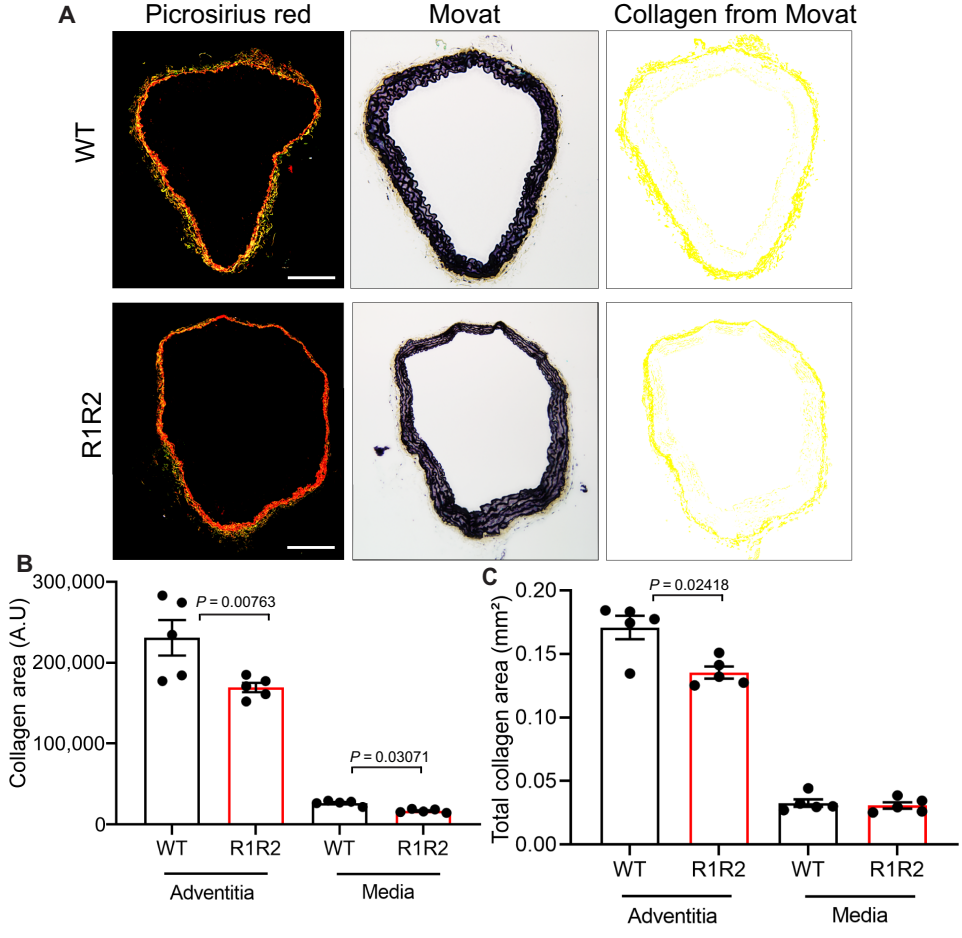

Fig. 8. ECM in R1R2 mutant aorta. (**A**) Picrosirius red staining (left) and total Movat's pentachrome staining (middle). Collagen content in Movat stains extracted by custom MATLAB software (*74*) (right) for ascending aortas from WT and R1R2 mutant mice at P24. Scale bar, 100 μm. (**B**) Quantification of total collagen fibers (red, orange, yellow, and green fibrils) identified by picrosirius red staining in the adventitia and media. Zoomed-in images are presented as fig. S9B. Values are means ± SEM of $N = 5$. Statistics analyzed by unpaired *t* test. (**C**) Quantification of total collagen area within adventitia and media of ascending aorta at P24 by Movat staining. Values are means ± SEM of $N = 5$. Statistics analyzed by unpaired *t* test.

A computational study also predicted force-dependent loosening of these interactions (*21*). While this point remains to be fully investigated, the notion that R1R2 separation occurs at a relatively early stage is consistent with available data.

The original R1R2 mutant that contained both interface and core mutations also showed increased formation of fibrillar adhesions and increased tension on talin. Both effects were diminished by vinculin depletion, consistent with increased vinculin recruitment to this mutant. These effects were not seen with talin constructs that contained interface mutations only, thus appearing to require domain unfolding and vinculin binding.

ARPC5L is a component of the ARP2/3 complex (*35*) and an ortholog of ARPC5. ARPC5L shares 68% identity with ARPC5, differing by insertion of six alanine residues in its N terminus (fig. S6A). The specific binding of ARPC5L suggests that this insert is required for binding to talin R2. Modeling of ARPC5L and talin R2 revealed an interaction between the free R2 domain and the six alanine residues in ARPC5L (fig. S6B), also seen with ARPC5L assembled in the ARP2/3 complex (fig. S6D). However, the reason for the higher binding of ARPC5L to the mutant versus WT R2-only is not entirely clear; there may be an accidental effect on affinity or on R2 conformation. Attempts to model this with AlphaFold2 did not yield any high confidence results. We recently developed a new method using a DNA clamp construct to apply tension to proteins on a biochemical scale and examined effects on R1R2 (*36*). This study directly demonstrated increased binding of ArpC5L to R1R2 under tension, confirming the results of the current study. Additional support derives from a proteomic study that identified ARPC5L (or ARP5L) in the focal adhesion proteome of blebbistatin-treated fibroblasts along with other ARP2/3 components (*37*).

Previous studies identified interactions of the ARP2/3 complex with vinculin and FAK (*38*–*40*) that reportedly regulate cell migration and lamellipodia formation. During migration, interaction of FAK with the ARP2/3 complex was found to be important for haptosensing of ECM concentration but not for ECM stiffness sensing (*41*). Melanoblasts derived from *Arp3* knockout mouse embryos also displayed decreased spreading on soft tissues and loss of cell-ECM contacts on stiffer tissues (*42*). Identification of a novel tension-sensitive interaction between talin and ARP2/3 thus strengthens the case for a key role of this actin regulator in cell adhesion.

Talin 1 was identified as a potential causal gene in sporadic TAAs including some variations that localized to R1R2, though whether ARPC5L is involved is unknown (*43*). Talin 1 was also reported to be a susceptibility gene for spontaneous coronary artery dissection (*44*) and to be down-regulated in aortic dissections (*45*). While these disease connections remain to be confirmed by functional analyses and larger-scale genetic studies, they lend support to a role for talin in mechanical homeostasis of arteries. One surprising result was the specificity for the ascending relative to the descending aorta. This effect could be due to the distinct embryonic lineages of vascular smooth muscle cells in these segments (*46*). In addition, because each contraction of the heart pulls down on the ascending aorta, this segment undergoes both axial and circumferential strain during the cardiac cycle, noting that axial changes are often the earliest in arterial adaptation and maladaptation (*47*). By contrast, the descending thoracic aorta undergoes only circumferential strain (*48*). To what extent these developmental and biomechanical differences account for the difference in talin-dependent matrix assembly remains to be determined.

In our study, we observed changes in aortic composition and properties in R1R2 mutant mice at P24. This age was chosen as a stage in postnatal development when elastin lamellae in the aortic media are fully formed but pressure-induced collagen organization and compensatory mechanisms are continuing to emerge (*12*). Lower axial stiffness was associated with lower content of fibrillar collagen in both the adventitia and media, suggesting that more than one cell type is affected. How ECM structure and content will evolve with age in the presence of compromised stiffness sensing is an ongoing question.

Limitations of our current study include unintended consequences of mutations within the R1R2 region, for example, alterations in binding to additional components. As the R1R2 interaction contributes to the stability of both the R1 and R2 domains, these mutations may reduce the force necessary to unfold either one. Binding of ARPC5L to R2 is predicted to block the R1R2 interaction and to stabilize R2, which may affect other processes. Recruitment of ARPC5L to talin may affect ARP2/3 functions in other regions of the cells. Mice with R1R2 interface mutations were examined at a single age chosen to minimize adaptation to altered talin function, but compensatory or pathological mechanisms cannot be excluded.

In summary, our work identified the R1R2 talin module as a critical stiffness regulator that triggers downstream stiffness-sensing responses through ARPC5L. The R1R2 mutant mice show subtle but significant differences in aortic ECM and mechanics in young mice. Important questions for future work include identifying pathways that link stiffness sensing to ECM gene expression, deposition, assembly, and turnover; contributions of substrate-stiffness sensing in mechanical homeostasis in other tissues; how this pathway participates in age-related artery stiffening; and how homeostatic regulation fails in diseases such as aneurysms and arteriosclerosis.

MATERIALS AND METHODS

Cell culture

Tln1$^{-/-}$ MEFs (*49*) were cultured as previously described (*18*). Briefly, MEFs were grown in cultured Dulbecco's modified Eagle's medium/F12 with 10% fetal bovine serum, penicillin-streptomycin, 0.001% β-mercaptoethanol, and 0.12% sodium bicarbonate. CRISPR-Cas9 deletion of vinculin in *Tln1*$^{-/-}$ MEFs used the vinculin-specific guide RNAs (sgNT 5′-GCGAGGTATTCGGCTCCGCG-3′; sgVinculin 5′-388 GCCGTCAGCAACCTCGTCC-3′) and procedures as previously described (*50*). ARPC5L was depleted in Tln1$^{-/-}$ MEFs using ON-TARGETplus SMART pool mouse ARPC5L siRNA (L-045648-01-0005; Horizon Discovery) alongside a Nontargeting control siRNA (D-001810-10-05; Horizon Discovery), using Lipofectamine RNAiMax transfection reagent (Thermo Fisher Scientific) as per the manufacturer's instructions. These cells were cultured in *Tln1*$^{-/-}$ MEFs media with puromycin (1 μg/ml). All cells were maintained in a humidified 37°C, 5% CO_2 incubator.

Plasmids and transfection

The R1R2, R3, and R10 mutant fragments as well as the R1R2 core and interface mutations were inserted in the previously described full-length talin-TS (*18*) by Gibson assembly. Rod-domain fragments for circular dichroism: His-tagged R1R2 WT, R1R2 (L638, L716T, A718D, and V722R) mutant, R3 WT and mutant (I805T) [similar to I805S in (*51*)], and R10 WT and mutant (L1923A), as well as R1R2 interface WT and mutant fragments were inserted into

Ptrc-His A vector, expressed in BL21(DE3) *Escherichia coli*, and purified on a Ni-NTA column as previously described (*52*). For coimmunoprecipitation, Flag-tagged ARPC5L was generated from pLVX GFP-ARPC5L (*35*) and GFP-tagged R1R2 WT and mutant fragments as well as R1 and R2 WT and mutant fragments were inserted in pLPCX vector. All cells were seeded 1 day before transfection and transfected using Lipofectamine 2000 (Thermo Fisher Scientific) as per the manufacturer's instructions. Cells were used in experiments 36 hours after transfection.

Circular dichroism, FRET, and FRAP

Circular dichroism was used to assess the stability of talin rod-domain constructs. Measurements were conducted using 100 μM talin fragment (WT, R1R2, R3, or R10 mutants) dissolved in buffer containing 50 mM KCl and 10 mM MES, pH 6.1. Spectra were recorded on a Jasco J-1100 CD spectrometer for the temperature intervals 10° to 70°C and 20° to 80°C for R1R2, R3, and R10, respectively, using a 1-mm path length and from wavelength range 250 to 180 nm. Spectra were collected every 5°C, with a temperature equilibration delay of 5 min. The scan rate was 100 nm/min, and three accumulations per sample were averaged to enhance sensitivity. Melting temperatures were evaluated from the maximum of the first derivative of the temperature dependence of the ellipticity at 220 nm.

FRAP experiments to assess talin turnover were performed on a Leica SP8 confocal microscope equipped with a FRAP module using a 63×, 1.4 NA (numerical aperture) oil objective. Cells were maintained at 37°C with humidity and CO_2 control. Images were acquired using LASX software. Three prebleach images at 2-s intervals and then a laser pulse at 100% power of the 488-nm line were used to bleach focal adhesions. Time-lapse images were acquired every 20 s for 9 min. Images were corrected for photobleaching during image analysis and normalized FRAP curves were plotted (*18*, *53*).

FRET imaging and analysis to measure tension on talin WT and mutant forms was performed as previously described (*18*). Briefly, *Tln1*$^{-/-}$ MEFs transfected with WT and mutant rod-domain plasmids were plated for 6 hours on fibronectin-coated glass-bottom dishes. Images were acquired using a 100×, 1.4 NA oil objective of a Nikon TiEclipse in the donor, acceptor, and FRET channels and normalized FRET index was calculated using a customized MATLAB code.

Focal adhesion morphology, fibronectin deposition, and stiffness-sensing assays

To assess focal adhesion morphology, cells transfected with GFP-tagged WT or mutant talin were seeded for 6 hours on glass-bottom dishes coated with fibronectin at 10 μg/ml, then fixed with 4% paraformaldehyde. Cells were imaged using a 60×, 1.4 NA oil objective on a Nikon Eclipse Ti microscope and focal adhesion areas were analyzed by ImageJ. Colocalization of WT and mutant talin was performed by immunostaining with antibodies against phospho-paxillin (rabbit; 44-722G; Thermo Fisher Scientific), vinculin (mouse, V9264, Sigma), and phospho-myosin light chain 2 (ser19) (rabbit; 3671; Cell Signaling Technology). For fibrillar adhesion analysis, *Tln1*$^{-/-}$ MEFs expressing WT and R1R2 mutant talin were grown for 48 hours on glass-bottom dishes, fixed with 4% paraformaldehyde, and stained for tensin-1 (rabbit; SAB4200283; Sigma-Aldrich; 1:300). Central focal adhesions are defined as all the adhesions that are in the cell center or peri-nuclear region of the cell present at least 5 μm away from the cell periphery (*18*). Note that the cell periphery was determined by the cytosolic talin intensity. Tensin1 fluorescence intensity was measured in these central adhesion regions. For fibronectin deposition, cells were grown for 48 hours on glass-bottom dishes, fixed with 4% paraformaldehyde, and stained for fibronectin using rabbit fibronectin (rabbit; F3648; Sigma-Aldrich; 1:300). Cells were counterstained with phalloidin to obtain cell boundaries. The fibronectin signal under each transfection positive cell was quantified using ImageJ.

Fibronectin fibrillogenesis was assayed biochemically as previously described (*54*). Briefly, *Tln1*$^{-/-}$ mouse embryo fibroblasts (MEFS) expressing WT and R1R2 talin were grown on 10-cm dishes for 48 hours and washed in ice-cold phosphate-buffered saline (PBS). Cells were lysed in a solubilization buffer, pH 8.8 [deoxycholate (2%), tris-HCl (25 mM), phenylmethylsulfonyl fluoride (PMSF; 2 mM), iodoacetic acid (2 mM), *N*-ethylmaleimide (2 mM), and EDTA (2 mM)]. The insoluble fraction was pelleted at 16,000*g* for 15 min. The pellet was solubilized in SDS (2%), tris-HCl (25 mM), PMSF (2 mM), iodoacetic acid (2 mM), *N*-ethylmaleimide (2 mM), and EDTA (2 mM), pH 8.0. The proteins were mixed with 4× Laemmli buffer (Bio-Rad), denatured at 95°C for 10 min, resolved on 8% SDS–polyacrylamide gel electrophoresis (SDS-PAGE) gel, and analyzed by Western blotting. The blots were incubated with anti-fibronectin antibody (rabbit; F3648; Sigma-Aldrich; 1:1000) overnight at 4°C followed by incubation with horseradish peroxidase (HRP)–conjugated anti-rabbit immunoglobulin G (IgG) (goat; PI-1000-1; Vector Labs; 1:5000), and proteins bands were visualized by chemiluminescence.

For stiffness-sensing assays, hydrogel substrates of varying stiffness were generated as previously described (*55*), by varying the acrylamide-bisacrylamide ratios. Fibronectin was covalently linked to the gels premixed with *N*-hydroxysuccinimide ester (1 mg/ml; 6066-82-6; Chemcruz) by overnight incubation at 4°C. The gels were then washed with PBS and equilibrated in cell culture media 1 hour before seeding. Cells were plated on these gels for 6 hours, followed by fixing with 4% paraformaldehyde and staining with rhodamine-phalloidin to image the cell body or with anti-YAP antibody (mouse; sc-101199, Santa Cruz Biotechnology; 1:300) to determine Yap nuclear localization.

Traction force microscopy

Traction force microscopy to assess cellular forces was performed as previously described (*18*). A thin layer of PDMS substrate on glass-bottom dishes was prepared by spin-coating. Three-kilopascal stiffness substrates were made by mixing a 1:1 ratio of silicone and curing agent (CY-52-276A and CY-52-276B; Dow Corning). Thirty-kilopascal stiffness substrates were prepared by mixing a base and curing agent from Sylgard 184 (Dow Corning) in a 40:1 ratio. The surface of the PDMS substrate was silanized using 3-aminopropyltriethoxy silane and a bead solution comprising borate buffer, pH 7.4, and 0.2-μm fluorescent beads (F-8807, Invitrogen, Molecular Probes) (1:2500 beads: buffer; v/v), and 1-ethyl-3-(3-dimethylaminopropyl) carbodiimide (0.1 mg/ml) was added for 2 hours at room temperature. The surface was then coated with fibronectin (10 μg/ml) overnight at 4°C. Cells were seeded and allowed to spread for 6 hours. Images of the beads with cells and after treatment with 0.1% SDS were acquired, and traction forces were calculated using custom-written MATLAB code (*56*, *57*).

Mass spectrometry

Plasmids encoding GFP, GFP-tagged R1R2, or GFP-tagged R2 WT constructs were expressed in 50% confluent HEK293T cells in a 100-mm dish using Lipofectamine 2000 as per the manufacturer's protocol. Thirty-six hours after transfections, cells were lysed in buffer containing 25 mM tris, pH 7.4, 1% NP-40, 150 mM NaCl, 0.1% bovine serum albumin (BSA), and 1× protease and phosphatase inhibitor cocktail (Thermo Fisher Scientific) at 4°C for 30 min. Proteins were immunoprecipitated using GFP-Trap beads (ChromoTek) overnight, followed by one wash in high-salt buffer (25 mM tris, pH 7.4, 1% NP-40, and 300 mM NaCl) and two washes in 25 mM tris, pH 7.4, 1% NP-40, and 150 mM NaCl. Proteins were eluted in 1× Laemmli buffer (Bio-Rad) and heated to 95°C for 5 min. The samples were loaded on 4 to 20% SDS tris-glycine gradient gels (Bio-Rad). When samples entered the gel by ~1 cm, the run was halted, and the gel was fixed in ethanol/acetic acid/water solution (3:1:6 v/v). The gel plug was excised and submitted to the Keck MS & Proteomics Resource at Yale School of Medicine for liquid chromatography–tandem mass spectrometry (LC-MS/MS) analysis to identify interacting partners.

Briefly, excised SDS-PAGE gel corresponding to coimmunoprecipitated proteins was fixed with methanol/water/acetonitrile (MeOH/H_2O/CAN) (45/45/10) and washed with water and 100 mM ammonium bicarbonate in 50/50 ACN/H_2O solution. Gel plugs were then treated with 4.5 mM DTT (20 min at 37°C, then allowed to cool to room temperature) and alkylated with iodoacetamide (for 20 min at room temperature in the dark). They were washed with (i) 100 mM ammonium bicarbonate in 50/50 ACN/H_2O solution, (ii) 25 mM ammonium bicarbonate in 50/50 ACN/H_2O solution, then with (iii) 100% acetonitrile solution before complete drying using the SpeedVac. Trypsin was added to the dried gel plug for enzymatic digestion in situ at 37°C overnight. Tryptic peptides were then extracted with 500 µl of 0.1% trifluoroacetic acid in 80/20 ACN/H_2O for 15 min; solutions were transferred to a new tube and dried in a SpeedVac. These digests were reconstituted in Buffer A and the resulting supernatant was injected onto a Waters nanoACQUITY UPLC coupled to a Q-Exactive Plus mass spectrometer containing a Waters Symmetry C18 180 µm × 20 mm trap column and a 1.7 µm, 75 µm × 250 mm nanoACQUITY UPLC column (35°C) for peptide separation. Peptide-trapping was performed at 5 µl/min with 99% Buffer A (100% water, 0.1% formic acid) and peptide separation at 300 nl/min with Buffer A and Buffer B (100% CH_3CN, 0.075% formic acid). High-energy collisional dissociation MS/MS spectra filtered by dynamic exclusion was acquired for the MS and MS/MS Q-Exactive Plus data collection. Orbitrap was used to detect all MS (Profile) and MS/MS (centroid) peaks. Resulting data-dependent LC-MS/MS data were analyzed using Proteome Discoverer 2.4 (Thermo Fisher Scientific) for peak picking and with Mascot search engine (v. 2.7 Matrix Science LLC) for database search with results imported into Scaffold (v. 4.0, Proteome Software) for further visual inspection and analyses. Two or more unique peptides per protein were considered positive hits with a Mascot Score greater than 95% confidence level. The mass spectrometry proteomics data have been deposited to the ProteomeXchange Consortium via the PRIDE (*58*) partner repository with the dataset identifier PXD041630.

Animals

All protocols involving live mice, including generation of talin R1R2 mutant knock-in mice and all experimental procedures were approved by the Yale University Institutional Animal Care and Use Committee (approval number 2023-20148).

Generation of mutant mice

The talin 1 L638D/V722R R1R2 mutant (R1R2 mutant) mice were generated stepwise via CRISPR-Cas9–based gene editing (*59*–*62*). Single guide RNA (sgRNA) selection was performed as follows. Potential Cas9 target guide (protospacer) sequences in the vicinity of the L638 and V722 codons, on exons 17 and 19 respectively, were screened using the online tool CRISPOR, http://crispor.tefor.net (*63*), and candidates were selected. Templates for sgRNA synthesis were generated by PCR from a pX330 template (Addgene). sgRNAs were transcribed in vitro and purified (MEGAshortscript, MEGAClear; Thermo Fisher Scientific). sgRNA/Cas9 RNPs were complexed and tested for activity by electroporation of zygotes, incubation of embryos to blastocyst stage, and genotyping of indels at the target sites. The sgRNAs that demonstrated the highest activity were selected. Guide RNA (gRNA) sequences were as follows: 5′ guide: GCCCCGTCAGAACCTGCTGC and 3′ guide: ACTAGCTGTTCTTGGCACAC. On the basis of these choices, a 1.6-kb long single-stranded DNA (lssDNA) recombination template containing the exon and intron regions between exons 17 and 19 and incorporating the L638D and V722R changes was synthesized (Integrated DNA Technologies). The sgRNA/Cas9 RNPs and homology template (lssDNA) mix were then microinjected into the pronuclei of C57BL/6J zygotes as previously described (*61*). Embryos were transferred to the oviducts of pseudo-pregnant CD-1 foster females using standard techniques. To identify the desired base changes, genotype screening of tissue biopsies from founder pups was performed by PCR amplification and Sanger sequencing. In the first round, only the L638D change was incorporated, thus, founder mice with that change were bred and their offspring were used as embryo donors for a second round of targeting. In the second round, only the 3′ sgRNA/Cas9 RNPs and a 148-base oligonucleotide were electroporated (*60*) to generate the double mutant L638D/V722R allele in the off-spring. The desired base changes were confirmed as described above. Germline transmission of the correctly targeted allele (i.e., both changes in the same allele) was confirmed by breeding and sequence analysis.

Atomic force microscopy

Mechanical properties in aortas from P24 mice were determined using AFM as previously described (*64*). A patch (≈5 mm^2) of tissue from the ascending or descending aorta was attached to a coverslip, with the adventitial surface facing upward. All experiments were performed in Hepes-buffered solution, pH 7.4. Measurements were obtained on a Bruker MultiMode 8 AFM in contact mode using a cantilever (PFQNM-LCA-CAL, Bruker) (*65*, *66*) with a tip radius of 70 nm and a nominal spring constant of 0.1 N/m. Force-deflection curves were obtained using the Nanoscope III Analysis software for each aorta at two different areas per aorta. The data obtained were fit using a Hertzian model (*67*) to obtain a compressive elastic modulus under small indentations.

Passive biomechanics and burst pressure tests

Standard biaxial biomechanical testing was performed as previously described (*68*). Briefly, the ascending thoracic aorta (from the root to the brachiocephalic artery) and the descending thoracic aorta (from first to fifth pairs of intercostal arteries) were isolated from P24 mice, cleaned of perivascular tissue, and their branches were ligated with a 7–0 nylon suture to allow ex vivo pressurization. The aortas were mounted

on glass cannulas and placed in a custom computer-controlled biaxial testing system, with temperature and pH maintained at physiological levels. Following four preconditioning cycles of pressurization and de-pressurization from 10 to 90 mmHg (noting that resting blood pressure is 70 to 80 mmHg at this age) at the energetically preferred in vivo axial stretch, four cyclic pressure-diameter tests and three cyclic axial force-length tests were performed. The unloading portion of the last cycle of all seven pressure-diameter and axial force-length tests were fit simultaneously with a microstructurally motivated four-fiber family nonlinear stored energy function, as previously described (*69*). Values of mean biaxial wall stress and material stiffness were computed from the stored energy function and calculated at multiple values of transmural pressure (e.g., 70 mmHg ex vivo, which is ~80 to 85 mmHg equivalent in vivo luminal pressure, and 90 mmHg ex vivo). Next, the samples were re-cannulated on a custom blunt-ended double-needle assembly, stretched to the estimated in vivo axial length, and pressurized until failure to determine burst pressure (*70*), an indicator of wall strength.

Histology

Aortas were fixed in 4% paraformaldehyde overnight, transferred to ethanol, embedded in paraffin, and 10-μm sections were cut. Sections were deparaffinized in xylene followed by washes in 95% to 70% ethanol gradient. For picrosirius red (Abcam, ab150681) and Movat pentachrome staining (Abcam, ab245884), slides were stained as per the manufacturer's instructions. For immunostaining for collagen III, antigen was retrieved by heating to 95°C in antigen retrieval buffer (Vector Labs, H-3300), followed by permeabilization in 0.025% Triton X-100 in PBS and blocking overnight in 10% donkey serum and 1% BSA. Sections were incubated overnight at 4°C with collagen III primary antibody (rabbit; ab7778; Abcam; 1:100), rinsed in TBS, pH 7.4, incubated with HRP-conjugated anti-rabbit IgG (goat; ab97080; Abcam; 1:500) for 1 hour at room temperature, and rinsed. Slides were developed using 3,3′-diaminobenzidine (Abcam; ab64238).

AlphaFold structural modeling

To produce the structural model of mouse R2 in complex with ARPC5L, ColabFold (*71*) was used to run the 3D protein structure prediction tool, AlphaFold (*72*). The R2 and ARPC5L sequences were submitted to the software, structural models were visualized in PyMOL, and compared against the crystal structure of mouse R1R2 [Protein Data Bank accession no. 1SJ8 (*31*)] and the cryo–electron microscopy structure of the ARP2/3 1B5CL complex [Protein Data Bank accession no. 6YW6 (*73*)]. All figures were made using PyMOL (Version 2.5.7; Schrödinger LLC).

Statistical analysis

Statistical analysis was performed using GraphPad Prism version 8 (GraphPad Software Inc.) or Origin (OriginLab Corp.) with actual *P* values showing statistical significance presented on graphs. Data were analyzed by unpaired Student's *t* test, Mann-Whitney test, or one-way analysis of variance (ANOVA) with Kruskal-Wallis post hoc test, two-way ANOVA with Tukey's post hoc test, or χ^2 analysis as indicated in the figure legends.

Supplementary Materials

This PDF file includes:
Figs. S1 to S10
Legends for tables S1 and S2

Other Supplementary Material for thismanuscript includes the following:
Tables S1 and S2

REFERENCES AND NOTES

1. J. D. Humphrey, E. R. Dufresne, M. A. Schwartz, Mechanotransduction and extracellular matrix homeostasis. *Nat. Rev. Mol. Cell Biol.* **15**, 802–812 (2014).
2. J. Herrera, C. A. Henke, P. B. Bitterman, Extracellular matrix as a driver of progressive fibrosis. *J. Clin. Invest.* **128**, 45–53 (2018).
3. R. D. Bülow, P. Boor, Extracellular matrix in kidney fibrosis: More than just a scaffold. *J. Histochem. Cytochem.* **67**, 643–661 (2019).
4. J. D. Humphrey, M. A. Schwartz, Vascular mechanobiology: Homeostasis, adaptation, and disease. *Annu. Rev. Biomed. Eng.* **23**, 1–27 (2021).
5. Y. Wang, P. Gao, F. Li, J. Du, Insights on aortic aneurysm and dissection: Role of the extracellular environment in vascular homeostasis. *J. Mol. Cell. Cardiol.* **171**, 90–101 (2022).
6. D. M. Milewicz, K. Michael, N. Fisher, J. S. Coselli, T. Markello, A. Biddinger, Fibrillin-1 (FBN1) mutations in patients with thoracic aortic aneurysms. *Circulation* **94**, 2708–2711 (1996).
7. D. C. Guo, H. Pannu, V. Tran-Fadulu, C. L. Papke, R. K. Yu, N. Avidan, S. Bourgeois, A. L. Estrera, H. J. Safi, E. Sparks, D. Amor, L. Ades, V. McConnell, C. E. Willoughby, D. Abuelo, M. Willing, R. A. Lewis, D. H. Kim, S. Scherer, P. P. Tung, C. Ahn, L. M. Buja, C. S. Raman, S. S. Shete, D. M. Milewicz, Mutations in smooth muscle α-actin (ACTA2) lead to thoracic aortic aneurysms and dissections. *Nat. Genet.* **39**, 1488–1493 (2007).
8. V. Tran-Fadulu, H. Pannu, D. H. Kim, G. W. Vick III, C. M. Lonsford, A. L. Lafont, C. Boccalandro, S. Smart, K. L. Peterson, J. Z. Hain, M. C. Willing, J. S. Coselli, S. A. LeMaire, C. Ahn, P. H. Byers, D. M. Milewicz, Analysis of multigenerational families with thoracic aortic aneurysms and dissections due to TGFBR1 or TGFBR2 mutations. *J. Med. Genet.* **46**, 607–613 (2009).
9. C. Bellini, S. Wang, D. M. Milewicz, J. D. Humphrey, Myh11$^{R247C/R247C}$ mutations increase thoracic aorta vulnerability to intramural damage despite a general biomechanical adaptivity. *J. Biomech.* **48**, 113–121 (2015).
10. H. Pannu, V. T. Fadulu, J. Chang, A. Lafont, S. N. Hasham, E. Sparks, P. F. Giampietro, C. Zaleski, A. L. Estrera, H. J. Safi, S. Shete, M. C. Willing, C. S. Raman, D. M. Milewicz, Mutations in transforming growth factor-β receptor type II cause familial thoracic aortic aneurysms and dissections. *Circulation* **112**, 513–520 (2005).
11. L. Wang, D. C. Guo, J. Cao, L. Gong, K. E. Kamm, E. Regalado, L. Li, S. Shete, W. Q. He, M. S. Zhu, S. Offermanns, D. Gilchrist, J. Elefteriades, J. T. Stull, D. M. Milewicz, Mutations in myosin light chain kinase cause familial aortic dissections. *Am. J. Hum. Genet.* **87**, 701–707 (2010).
12. S. I. Murtada, Y. Kawamura, G. Li, M. A. Schwartz, G. Tellides, J. D. Humphrey, Developmental origins of mechanical homeostasis in the aorta. *Dev. Dyn.* **250**, 629–639 (2021).
13. J. D. Humphrey, Mechanisms of arterial remodeling in hypertension. *Hypertension* **52**, 195–200 (2008).
14. A. Moro, T. P. Driscoll, L. C. Boraas, W. Armero, D. M. Kasper, N. Baeyens, C. Jouy, V. Mallikarjun, J. Swift, S. J. Ahn, D. Lee, J. Zhang, M. Gu, M. Gerstein, M. Schwartz, S. Nicoli, MicroRNA-dependent regulation of biomechanical genes establishes tissue stiffness homeostasis. *Nat. Cell Biol.* **21**, 348–358 (2019).
15. J. Z. Kechagia, J. Ivaska, P. Roca-Cusachs, Integrins as biomechanical sensors of the microenvironment. *Nat. Rev. Mol. Cell Biol.* **20**, 457–473 (2019).
16. M. Yao, B. T. Goult, B. Klapholz, X. Hu, C. P. Toseland, Y. Guo, P. Cong, M. P. Sheetz, J. Yan, The mechanical response of talin. *Nat. Commun.* **7**, 11966 (2016).
17. J. Yan, M. Yao, B. T. Goult, M. P. Sheetz, Talin dependent mechanosensitivity of cell focal adhesions. *Cell Mol. Bioeng.* **8**, 151–159 (2015).
18. A. Kumar, M. Ouyang, K. Van den Dries, E. J. McGhee, K. Tanaka, M. D. Anderson, A. Groisman, B. T. Goult, K. I. Anderson, M. A. Schwartz, Talin tension sensor reveals novel features of focal adhesion force transmission and mechanosensitivity. *J. Cell Biol.* **213**, 371–383 (2016).
19. B. T. Goult, J. Yan, M. A. Schwartz, Talin as a mechanosensitive signaling hub. *J. Cell Biol.* **217**, 3776–3784 (2018).
20. S. E. Lee, R. D. Kamm, M. R. Mofrad, Force-induced activation of talin and its possible role in focal adhesion mechanotransduction. *J. Biomech.* **40**, 2096–2106 (2007).
21. V. P. Hytönen, V. Vogel, How force might activate talin's vinculin binding sites: SMD reveals a structural mechanism. *PLOS Comput. Biol.* **4**, e24 (2008).
22. A. del Rio, R. Perez-Jimenez, R. Liu, P. Roca-Cusachs, J. M. Fernandez, M. P. Sheetz, Stretching single talin rod molecules activates vinculin binding. *Science* **323**, 638–641 (2009).
23. B. T. Goult, T. Zacharchenko, N. Bate, R. Tsang, F. Hey, A. R. Gingras, P. R. Elliott, G. C. K. Roberts, C. Ballestrem, D. R. Critchley, I. L. Barsukov, RIAM and vinculin binding to talin are mutually exclusive and regulate adhesion assembly and turnover. *J. Biol. Chem.* **288**, 8238–8249 (2013).

24. A. R. Gingras, W. H. Ziegler, R. Frank, I. L. Barsukov, G. C. Roberts, D. R. Critchley, J. Emsley, Mapping and consensus sequence identification for multiple vinculin binding sites within the talin rod. *J. Biol. Chem.* **280**, 37217–37224 (2005).
25. A. Elosegui-Artola, R. Oria, Y. Chen, A. Kosmalska, C. Pérez-González, N. Castro, C. Zhu, X. Trepat, P. Roca-Cusachs, Mechanical regulation of a molecular clutch defines force transmission and transduction in response to matrix rigidity. *Nat. Cell Biol.* **18**, 540–548 (2016).
26. P. Atherton, B. Stutchbury, D. Y. Wang, D. Jethwa, R. Tsang, E. Meiler-Rodriguez, P. Wang, N. Bate, R. Zent, I. L. Barsukov, B. T. Goult, D. R. Critchley, C. Ballestrem, Vinculin controls talin engagement with the actomyosin machinery. *Nat. Commun.* **6**, 10038 (2015).
27. R. Rahikainen, T. Öhman, P. Turkki, M. Varjosalo, V. P. Hytönen, Talin-mediated force transmission and talin rod domain unfolding independently regulate adhesion signaling. *J. Cell Sci.* **132**, jcs226514 (2019).
28. E. Zamir, B. Geiger, Molecular complexity and dynamics of cell-matrix adhesions. *J. Cell Sci.* **114**, 3583–3590 (2001).
29. S. Dupont, Role of YAP/TAZ in cell-matrix adhesion-mediated signalling and mechanotransduction. *Exp. Cell Res.* **343**, 42–53 (2016).
30. P. W. Oakes, S. Banerjee, M. C. Marchetti, M. L. Gardel, Geometry regulates traction stresses in adherent cells. *Biophys. J.* **107**, 825–833 (2014).
31. E. Papagrigoriou, A. R. Gingras, I. L. Barsukov, N. Bate, I. J. Fillingham, B. Patel, R. Frank, W. H. Ziegler, G. C. Roberts, D. R. Critchley, J. Emsley, Activation of a vinculin-binding site in the talin rod involves rearrangement of a five-helix bundle. *EMBO J.* **23**, 2942–2951 (2004).
32. K. Austen, P. Ringer, A. Mehlich, A. Chrostek-Grashoff, C. Kluger, C. Klingner, B. Sabass, R. Zent, M. Rief, C. Grashoff, Extracellular rigidity sensing by talin isoform-specific mechanical linkages. *Nat. Cell Biol.* **17**, 1597–1606 (2015).
33. J. E. Wagenseil, R. P. Mecham, Vascular extracellular matrix and arterial mechanics. *Physiol. Rev.* **89**, 957–989 (2009).
34. M. Yao, B. T. Goult, H. Chen, P. Cong, M. P. Sheetz, J. Yan, Mechanical activation of vinculin binding to talin locks talin in an unfolded conformation. *Sci. Rep.* **4**, 4610 (2014).
35. J. V. Abella, C. Galloni, J. Pernier, D. J. Barry, S. Kjær, M. F. Carlier, M. Way, Isoform diversity in the Arp2/3 complex determines actin filament dynamics. *Nat. Cell Biol.* **18**, 76–86 (2016).
36. M. Chung, K. Zhou, J. Powell, C. Lin, M. A. Schwartz, A DNA-based molecular clamp for probing protein interactions and structure under force. bioRxiv 597759 [Preprint] (2024). https://doi.org/10.1101/2024.06.06.597759.
37. J. C. Kuo, X. Han, C. T. Hsiao, J. R. Yates III, C. M. Waterman, Analysis of the myosin-II-responsive focal adhesion proteome reveals a role for β-Pix in negative regulation of focal adhesion maturation. *Nat. Cell Biol.* **13**, 383–393 (2011).
38. K. A. DeMali, C. A. Barlow, K. Burridge, Recruitment of the Arp2/3 complex to vinculin. *J. Cell Biol.* **159**, 881–891 (2002).
39. B. Serrels, A. Serrels, V. G. Brunton, M. Holt, G. W. McLean, C. H. Gray, G. E. Jones, M. C. Frame, Focal adhesion kinase controls actin assembly via a FERM-mediated interaction with the Arp2/3 complex. *Nat. Cell Biol.* **9**, 1046–1056 (2007).
40. D. S. Chorev, O. Moscovitz, B. Geiger, M. Sharon, Regulation of focal adhesion formation by a vinculin-Arp2/3 hybrid complex. *Nat. Commun.* **5**, 3758 (2014).
41. V. Swaminathan, R. S. Fischer, C. M. Waterman, The FAK-Arp2/3 interaction promotes leading edge advance and haptosensing by coupling nascent adhesions to lamellipodia actin. *Mol. Biol. Cell* **27**, 1085–1100 (2016).
42. V. Papalazarou, K. Swaminathan, F. Jaber-Hijazi, H. Spence, I. Lahmann, C. Nixon, M. Salmeron-Sanchez, H.-H. Arnold, K. Rottner, L. M. Machesky, The Arp2/3 complex is critical for colonisation of the mouse skin by melanoblasts. *Development* **147**, dev194555 (2020).
43. Y. Li, S. Gao, Y. Han, L. Song, Y. Kong, Y. Jiao, S. Huang, J. Du, Y. Li, Variants of focal adhesion scaffold genes cause thoracic aortic aneurysm. *Circ. Res.* **128**, 8–23 (2021).
44. T. N. Turley, J. L. Theis, R. S. Sundsbak, J. M. Evans, M. M. O'Byrne, R. Gulati, M. S. Tweet, S. N. Hayes, T. M. Olson, Rare missense variants in *TLN1* are associated with familial and sporadic spontaneous coronary artery dissection. *Circ. Genom. Precis. Med.* **12**, e002437 (2019).
45. X. Wei, Y. Sun, Y. Wu, J. Zhu, B. Gao, H. Yan, Z. Zhao, J. Zhou, Z. Jing, Downregulation of talin-1 expression associates with increased proliferation and migration of vascular smooth muscle cells in aortic dissection. *BMC Cardiovasc. Disord.* **17**, 162 (2017).
46. M. W. Majesky, Developmental basis of vascular smooth muscle diversity. *Arterioscler. Thromb. Vasc. Biol.* **27**, 1248–1258 (2007).
47. R. L. Gleason, J. D. Humphrey, Effects of a sustained extension on arterial growth and remodeling: A theoretical study. *J. Biomech.* **38**, 1255–1261 (2005).
48. J. Ferruzzi, P. Di Achille, G. Tellides, J. D. Humphrey, Combining in vivo and in vitro biomechanical data reveals key roles of perivascular tethering in central artery function. *PLOS ONE* **13**, e0201379 (2018).
49. H. Priddle, L. Hemmings, S. Monkley, A. Woods, B. Patel, D. Sutton, G. A. Dunn, D. Zicha, D. R. Critchley, Disruption of the talin gene compromises focal adhesion assembly in undifferentiated but not differentiated embryonic stem cells. *J. Cell Biol.* **142**, 1121–1133 (1998).
50. T. P. Driscoll, S. J. Ahn, B. Huang, A. Kumar, M. A. Schwartz, Actin flow-dependent and -independent force transmission through integrins. *Proc. Natl. Acad. Sci. U.S.A.* **117**, 32413–32422 (2020).
51. R. Rahikainen, M. von Essen, M. Schaefer, L. Qi, L. Azizi, C. Kelly, T. O. Ihalainen, B. Wehrle-Haller, M. Bastmeyer, C. Huang, V. P. Hytönen, Mechanical stability of talin rod controls cell migration and substrate sensing. *Sci. Rep.* **7**, 3571 (2017).
52. A. Spriestersbach, J. Kubicek, F. Schäfer, H. Block, B. Maertens, Chapter one—Purification of his-Tagged proteins, in *Methods in Enzymology*, J. R. Lorsch, Ed. (Academic Press, 2015), vol. 559, pp. 1–15.
53. L. M. Gallego-Paez, W. J. S. Edwards, M. Chanduri, Y. Guo, T. Koorman, C.-Y. Lee, N. Grexa, P. Derksen, J. Yan, M. A. Schwartz, J. Mauer, B. T. Goult, *TLN1* contains a cancer-associated cassette exon that alters talin-1 mechanosensitivity. *J. Cell Biol.* **222**, e202209010 (2023).
54. A. W. Orr, M. H. Ginsberg, S. J. Shattil, H. Deckmyn, M. A. Schwartz, Matrix-specific suppression of integrin activation in shear stress signaling. *Mol. Biol. Cell* **17**, 4686–4697 (2006).
55. T. P. Driscoll, T. C. Bidone, S. J. Ahn, A. Yu, A. Groisman, G. A. Voth, M. A. Schwartz, Integrin-based mechanosensing through conformational deformation. *Biophys. J.* **120**, 4349–4359 (2021).
56. A. F. Mertz, S. Banerjee, Y. Che, G. K. German, Y. Xu, C. Hyland, M. C. Marchetti, V. Horsley, E. R. Dufresne, Scaling of traction forces with the size of cohesive cell colonies. *Phys. Rev. Lett.* **108**, 198101 (2012).
57. A. F. Mertz, Y. Che, S. Banerjee, J. M. Goldstein, K. A. Rosowski, S. F. Revilla, C. M. Niessen, M. C. Marchetti, E. R. Dufresne, V. Horsley, Cadherin-based intercellular adhesions organize epithelial cell-matrix traction forces. *Proc. Natl. Acad. Sci. U.S.A.* **110**, 842–847 (2013).
58. Y. Perez-Riverol, J. Bai, C. Bandla, D. García-Seisdedos, S. Hewapathirana, S. Kamatchinathan, D. J. Kundu, A. Prakash, A. Frericks-Zipper, M. Eisenacher, M. Walzer, S. Wang, A. Brazma, J. A. Vizcaíno, Vizcaíno, the PRIDE database resources in 2022: A hub for mass spectrometry-based proteomics evidences. *Nucleic Acids Res.* **50**, D543–D552 (2021).
59. H. Yang, H. Wang, R. Jaenisch, Generating genetically modified mice using CRISPR/Cas-mediated genome engineering. *Nat. Protoc.* **9**, 1956–1968 (2014).
60. S. Chen, B. Lee, A. Y. Lee, A. J. Modzelewski, L. He, Highly efficient mouse genome editing by CRISPR ribonucleoprotein electroporation of zygotes. *J. Biol. Chem.* **291**, 14457–14467 (2016).
61. R. M. Quadros, H. Miura, D. W. Harms, H. Akatsuka, T. Sato, T. Aida, R. Redder, G. P. Richardson, Y. Inagaki, D. Sakai, S. M. Buckley, P. Seshacharyulu, S. K. Batra, M. A. Behlke, S. A. Zeiner, A. M. Jacobi, Y. Izu, W. B. Thoreson, L. D. Urness, S. L. Mansour, M. Ohtsuka, C. B. Gurumurthy, *Easi*-CRISPR: A robust method for one-step generation of mice carrying conditional and insertion alleles using Long ssDNA donors and CRISPR ribonucleoproteins. *Genome Biol.* **18**, 92 (2017).
62. N. L. Price, N. Rotllan, X. Zhang, A. Canfrán-Duque, T. Nottoli, Y. Suarez, C. Fernández-Hernando, Specific disruption of Abca1 targeting largely mimics the effects of miR-33 knockout on macrophage cholesterol efflux and atherosclerotic plaque development. *Circ. Res.* **124**, 874–880 (2019).
63. J. P. Concordet, M. Haeussler, CRISPOR: Intuitive guide selection for CRISPR/Cas9 genome editing experiments and screens. *Nucleic Acids Res.* **46**, W242–W245 (2018).
64. Y. H. Bae, S. L. Liu, F. J. Byfield, P. A. Janmey, R. K. Assoian, Measuring the stiffness of ex vivo mouse aortas using atomic force microscopy. *J. Vis. Exp.* **19**, 54630 (2016).
65. H. Schillers, I. Medalsy, S. Hu, A. L. Slade, J. E. Shaw, PeakForce tapping resolves individual microvilli on living cells. *J. Mol. Recognit.* **29**, 95–101 (2016).
66. J. Rodriguez-Ramos, F. Rico, Determination of calibration parameters of cantilevers of arbitrary shape by finite element analysis. *Rev. Sci. Instrum.* **92**, 045001 (2021).
67. P. Carl, H. Schillers, Elasticity measurement of living cells with an atomic force microscope: Data acquisition and processing. *Pflügers Arch.* **457**, 551–559 (2008).
68. J. Ferruzzi, M. R. Bersi, J. D. Humphrey, Biomechanical phenotyping of central arteries in health and disease: Advantages of and methods for murine models. *Ann. Biomed. Eng.* **41**, 1311–1330 (2013).
69. J. Ferruzzi, M. R. Bersi, S. Uman, H. Yanagisawa, J. D. Humphrey, Decreased elastic energy storage, not increased material stiffness, characterizes central artery dysfunction in fibulin-5 deficiency independent of sex. *J. Biomech. Eng.* **137**, 0310071–03100714 (2015).
70. D. Weiss, B. V. Rego, C. Cavinato, D. S. Li, Y. Kawamura, N. Emuna, J. D. Humphrey, Effects of age, sex, and extracellular matrix integrity on aortic dilatation and rupture in a mouse model of marfan syndrome. *Arterioscler. Thromb. Vasc. Biol.* **43**, e358–e372 (2023).
71. M. Mirdita, K. Schütze, Y. Moriwaki, L. Heo, S. Ovchinnikov, M. Steinegger, ColabFold: Making protein folding accessible to all. *Nat. Methods* **19**, 679–682 (2022).
72. J. Jumper, R. Evans, A. Pritzel, T. Green, M. Figurnov, O. Ronneberger, K. Tunyasuvunakool, R. Bates, A. Žídek, A. Potapenko, A. Bridgland, C. Meyer, S. A. A. Kohl, A. J. Ballard, A. Cowie, B. Romera-Paredes, S. Nikolov, R. Jain, J. Adler, T. Back, S.

Petersen, D. Reiman, E. Clancy, M. Zielinski, M. Steinegger, M. Pacholska, T. Berghammer, S. Bodenstein, D. Silver, O. Vinyals, A. W. Senior, K. Kavukcuoglu, P. Kohli, D. Hassabis, Highly accurate protein structure prediction with AlphaFold. *Nature* **596**, 583–589 (2021).
73. O. von Loeffelholz, A. Purkiss, L. Cao, S. Kjaer, N. Kogata, G. Romet-Lemonne, M. Way, C. A. Moores, Cryo-EM of human Arp2/3 complexes provides structural insights into actin nucleation modulation by ARPC5 isoforms. *Biol. open* **9**, (2020).
74. M. R. Bersi, C. Bellini, J. D. Humphrey, S. Avril, Local variations in material and structural properties characterize murine thoracic aortic aneurysm mechanics. *Biomech. Model. Mechanobiol.* **18**, 203–218 (2019).

Acknowledgments: We thank members of the Yale Genome Editing Center for generating the talin R1R2 mutant mice. We also thank G. Tellides and Q. Huang for help with mouse experiments. We thank the Keck MS & Proteomics Resource for providing the necessary mass spectrometers and the accompany biotechnology tools, which is partly funded by Yale School of Medicine and by the Office of the Director, National Institutes of Health (S10OD02365101A1, S10OD019967, and S10OD018034). We also thank Yale pathology tissue services for help with paraffin-embedding, sectioning, and staining of tissues. **Funding:** This work was supported by USPHS grant PO1 HL134605 to M.A.S. and J.D.H. **Author contributions:** M.C.: Investigation, methodology, conceptualization, resources, data curation, validation, formal analysis, visualization, validation, formal analysis, and writing (original draft, reviewing and editing). A.K.: Investigation, methodology, conceptualization, resources, data curation, validation, formal analysis, visualization, validation, formal analysis, software, project administration and supervision, and writing (original draft, reviewing and editing). D.W.: Investigation, methodology, resources, validation, formal analysis, project administration (biomechanical data), visualization, and writing (original draft, reviewing and editing). N.E.: Investigation, resources, validation, formal analysis, visualization, software, and writing (reviewing and editing). I.B.: Investigation, methodology, and resources. M.S.: Investigation, resources, validation, visualization, and writing (reviewing and editing). K.T.: Methodology. X.W.: Investigation, methodology, resources, and data curation. A.D.: Investigation, validation, and writing (original draft, reviewing and editing). J.K.: Investigation, resources, and data curation. F.C.: Investigation. T.L.: Investigation, methodology, resources, validation, data curation, supervision, and writing (reviewing and editing). U.D.S.: Project administration and supervision. S.B. and T.N.: Methodology and resources. B.T.G.: Methodology, formal analysis, visualization, conceptualization, and writing (reviewing and editing). J.D.H.: Methodology, resources, validation, formal analysis, visualization, conceptualization, project administration, supervision, and writing (reviewing and editing). M.A.S.: Conceptualization, methodology, funding acquisition, supervision, project administration, and writing (original draft, reviewing and editing). **Competing interests:** The authors declare that they have no competing interests. **Data and materials availability:** All data needed to evaluate the conclusions in the paper are present in the paper and/or the Supplementary Materials. The mass spectrometry proteomics data have been deposited to the ProteomeXchange Consortium with the dataset identifier PXD041630.

Submitted 8 May 2023
Accepted 16 July 2024
Published 21 August 2024
10.1126/sciadv.adi6286